



Landing Site Selection and Characterization of Tianwen-1 (Zhurong Rover) on Mars

Bo Wu¹ , Jie Dong², Yiran Wang¹, Wei Rao², Zezhou Sun², Zhaojin Li¹ , Zhiyun Tan², Zeyu Chen¹, Chuang Wang², Wai Chung Liu¹ , Long Chen¹ , Jiaming Zhu¹, and Hongliang Li¹

¹Planetary Remote Sensing Laboratory, Department of Land Surveying & Geo-Informatics, The Hong Kong Polytechnic University, Hong Kong, PR China, ²China Academy of Space Technology, Beijing, PR China

Key Points:

- Landing site selection for the Zhurong rover within a pre-identified landing region in southern Utopia Planitia
- Surface and shallow subsurface properties at the Zhurong landing site
- Multiple episodes of resurfacing at the landing region from crater size-frequency distribution analysis

Supporting Information:

Supporting Information may be found in the online version of this article.

Correspondence to:

B. Wu and J. Dong,
bo.wu@polyu.edu.hk;
donghn13@163.com

Citation:

Wu, B., Dong, J., Wang, Y., Rao, W., Sun, Z., Li, Z., et al. (2022). Landing site selection and characterization of Tianwen-1 (Zhurong rover) on Mars. *Journal of Geophysical Research: Planets*, 127, e2021JE007137. <https://doi.org/10.1029/2021JE007137>

Received 19 NOV 2021

Accepted 19 MAR 2022

Author Contributions:

Conceptualization: Bo Wu, Wei Rao, Zezhou Sun

Funding acquisition: Jie Dong, Wei Rao, Zezhou Sun, Zhiyun Tan

Investigation: Bo Wu, Jie Dong, Wei Rao, Zhaojin Li, Zeyu Chen, Wai Chung Liu, Jiaming Zhu, Hongliang Li

Methodology: Bo Wu, Jie Dong, Yiran Wang, Wei Rao, Zezhou Sun, Zhiyun Tan, Zeyu Chen, Chuang Wang, Wai Chung Liu, Jiaming Zhu

Project Administration: Bo Wu, Wei Rao, Zezhou Sun, Chuang Wang

Software: Yiran Wang, Zhaojin Li, Zhiyun Tan, Zeyu Chen, Chuang Wang, Wai Chung Liu, Long Chen, Jiaming Zhu, Hongliang Li

© 2022 The Authors.

This is an open access article under the terms of the [Creative Commons Attribution-NonCommercial License](https://creativecommons.org/licenses/by-nc/4.0/), which permits use, distribution and reproduction in any medium, provided the original work is properly cited and is not used for commercial purposes.

Abstract The Chinese Mars rover Zhurong onboard the Tianwen-1 probe successfully landed on Mars in May 2021. Here, we report our efforts in selecting a landing site for Zhurong within a pre-identified landing region in southern Utopia Planitia. Using the high-resolution images collected by a camera onboard the Tianwen-1 orbiter, the landing region was analyzed in detail in terms of surface slopes, crater densities and rock abundances, which enabled the optimized determination of a landing ellipse (56×22 km for the major and minor axes) with minimum hazards and assisted the successful landing of the Zhurong rover. We also characterized the landing site and region after landing. Surface images captured by a camera onboard the Zhurong rover revealed a low rock abundance of approximately 4% at the landing site, similar to the rock measurements from orbital data before landing. Images of the surface features and a hole excavated by the pulsed retrorockets beneath the lander suggested a shallow regolith structure with a surficial layer of dust and sand over a layer of duricrust, and brecciated/fragmented rocks and bedrocks beneath. Crater size-frequency distribution analysis indicated that the landing region might have experienced multiple episodes of resurfacing.

Plain Language Summary The Chinese Mars rover Zhurong onboard the Tianwen-1 probe successfully landed on Mars in May 2021. Here, we report our efforts in selecting a landing site for Zhurong within a pre-identified landing region in southern Utopia Planitia. Using the high-resolution images collected by a camera onboard the Tianwen-1 orbiter, the landing region was analyzed in detail in terms of surface slopes, crater densities and rock abundances, which enabled the optimized determination of a landing site with minimum hazards and assisted the successful landing of the Zhurong rover. We also characterized the landing site and region after landing. Surface images captured by a camera onboard the Zhurong rover revealed a low rock abundance at the landing site. Images of the surface features and a hole excavated by the pulsed retrorockets beneath the lander suggest a shallow regolith structure with a surficial layer of dust and sand over a layer of duricrust, and fragmented rocks and bedrocks beneath. Crater size-frequency distribution analysis suggested that the landing region might have experienced multiple episodes of resurfacing.

1. Introduction

China's first Mars rover, Zhurong, successfully landed in southern Utopia Planitia on the Martian surface (Figure 1) on 15 May 2021. Zhurong was onboard the Tianwen-1 probe, which was successfully launched on 23 July 2020; the probe entered the Martian orbit on 10 February 2021 and released the Zhurong rover for landing about 3 hr before its touchdown (Li et al., 2021; Wan et al., 2020; Wu et al., 2021). The Zhurong rover landing represents the tenth in situ investigation of the Martian surface and the first in the lowland area of southern Utopia Planitia. Using the scientific payloads onboard the Zhurong rover (Li et al., 2021), including the Navigation and Terrain Camera (NaTeCam), Multispectral Camera (MSCam), Mars Surface Composition Detector (MarSCoDe), Mars Rover Penetrating Radar (RoPeR), Mars Rover Magnetometer, and Mars Climate Station, the Zhurong rover will investigate the topography, soil structure and geology of the roving area and the physical characteristics of the atmosphere. The rover will also analyze elements, minerals and rock types and search for signatures of water or ice in the roving area (Li et al., 2021; Zou et al., 2021).

The landing site selection process for Zhurong included several stages. In the first stage, a global search process was conducted on the Martian surface to identify suitable regions that met the engineering constraints, including adequate solar illumination for generating power and warmth, lower elevation for a thicker atmosphere and longer deceleration time, and a flat terrain surface for safer landing (Dong et al., 2019; Wu et al., 2021). Three

Supervision: Wei Rao, Zezhou Sun
Validation: Jie Dong, Yiran Wang, Zhaojin Li, Long Chen
Writing – original draft: Bo Wu
Writing – review & editing: Bo Wu

candidate landing areas located within 5°–30°N were identified. They are located on the large plains on Mars, that is, Amazonis Planitia, Chryse Planitia and Utopia/Isidis Planitia. The landing area in Amazonis Planitia was ruled out owing to its small thermal inertias and possible thick dust. In the second stage, detailed analyses of the elevations, slopes, rock abundances, crater densities and geological context were conducted for the remaining two candidate landing areas. The area in Chryse Planitia was excluded owing to its relatively rough terrain surface and complicated geomorphological features. A local area in southern Utopia Planitia was further selected as the target landing area (109°–133°E and 23°–30°N; the cyan polygon in Figure 1) for its optimal combination of the above-mentioned factors (Wu et al., 2021). In the third stage, the target landing area was examined in detail in terms of engineering safety and scientific importance, and two local regions within the target landing area were short-listed, with one as the main landing region (approximately 180 × 70 km in size centered at 110.318°E, 24.748°N; the red polygon in Figure 1) and the other as a backup landing region (centered at 131.626°E, 26.467°N with similar size). Details of the above selection processes can be found in our previous works (Dong et al., 2019; Wu et al., 2021).

After the Tianwen-1 probe entered the Martian orbit on 10 February 2021, its onboard high-resolution imaging camera (HiRIC; Meng et al., 2021) collected high-resolution stereo images (0.7 m/pixel) covering the main landing region (the red polygon in Figure 1). In the last stage of the landing site selection process, we focused on the main landing region and conducted detailed topographic and geomorphological mapping and analysis within the region based on the HiRIC imagery from early March to early May 2021. Based on the results, several landing ellipses (of major and minor axes 56 and 22 km, respectively) within the main landing region were suggested to the mission team in early May 2021. The Zhurong rover successfully landed in the selected first-priority landing ellipse on 15 May 2021.

In this paper, we present our efforts in selecting the final landing site within the main landing region for the Zhurong rover. We also present the actual landing site and features of scientific interest in the nearby region. The characteristics of the landing region are investigated in terms of the surface and shallow subsurface properties as well as the age of the surface. The scientific implications of the findings are also discussed.

2. Landing Site Selection

2.1. Topographic Mapping and Slope Analysis

The HiRIC onboard the Tianwen-1 orbiter is a linear pushbroom camera that can collect images of the Martian surface with a spatial resolution of 0.7 m/pixel at an orbit height of 300 km (Meng et al., 2021). Stereo images covering the same region can be collected by tilting the orbiter platform at an angle of approximately 11.3° or –11.3° along the flight direction when the orbiter revisits the region (usually at a time interval of approximately 2 days). From 2 March to 16 April 2021, the HiRIC collected 21 strips of images (9 stereo pairs plus 3 strips as backup) covering the main landing region. Each image has a width of 18,432 pixels and a length of 240,000–285,000 pixels. The collected HiRIC images were used for topographic mapping and analysis of the main landing region. Figure 2a shows a digital elevation model (DEM) with a spatial resolution of 5 m/pixel, which was generated from the stereo HiRIC images using our in-house photogrammetric software (Hu & Wu, 2019). The HiRIC images with relatively low emission angles (Table S1 in Supporting Information S1) were further ortho-rectified based on the DEM to generate an image mosaic covering the main landing region shown as the background image in Figure 2.

The geometric accuracies of the generated image mosaic and DEM were evaluated by comparison with reference data. Mars Reconnaissance Orbiter (MRO) Context Camera (CTX) images were used to generate an image mosaic (6 m/pixel) covering the same area (Wu et al., 2021). The CTX images were map-projected based on the Mars Orbiter Laser Altimeter (MOLA) DEM and mosaicked by using our in-house photogrammetric software (Hu & Wu, 2019). A shaded relief of the MOLA DEM was generated and a number of surface features (e.g., centers of small craters) recognizable on both the CTX image mosaic and the MOLA shaded relief were selected. These features were evenly distributed across the region and they were used as control points to co-register the CTX image mosaic to the MOLA DEM with minimum offset. The CTX image mosaic was then used as a reference for evaluating the planimetric accuracies of the HiRIC image mosaic and the DEM. By manually selecting 42 common feature points on the HiRIC and CTX image mosaics along their boundaries and across their overlapping region, the planimetric accuracy of the former can be represented by the positional differences

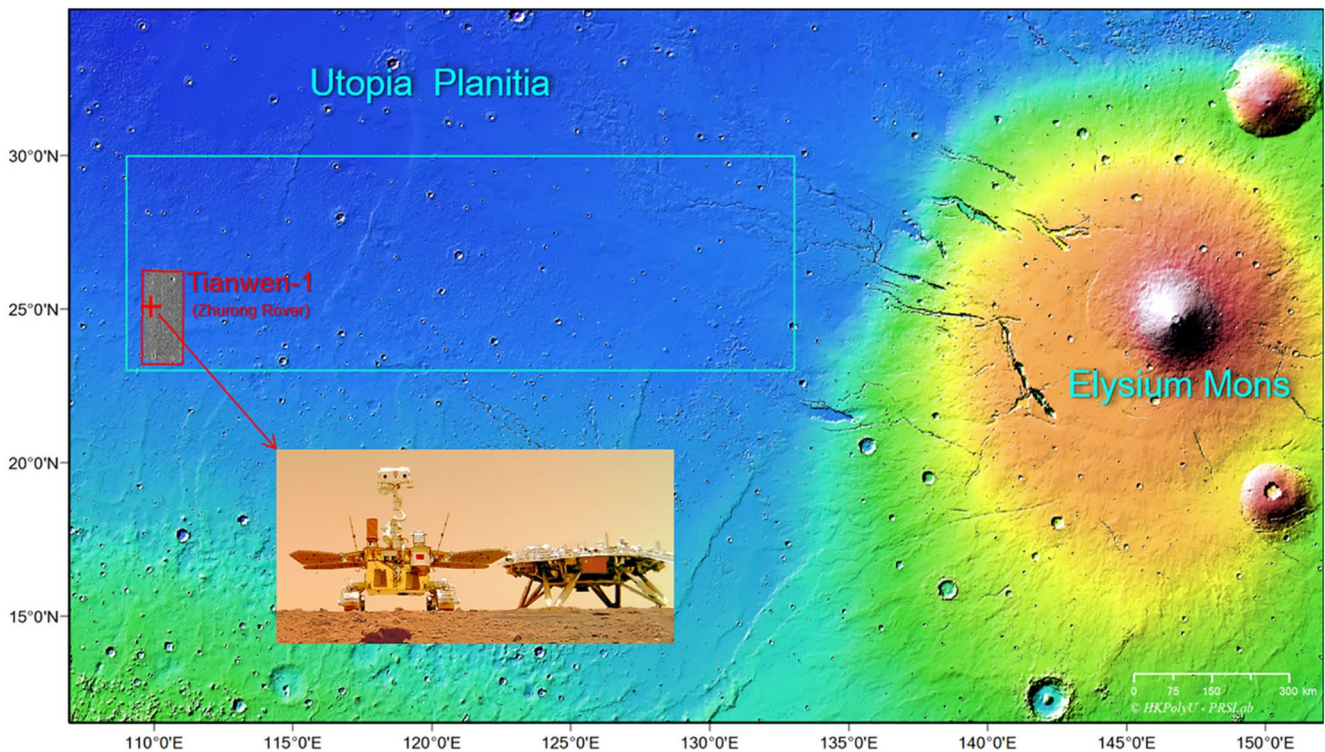


Figure 1. Landing site (red cross) of Tianwen-1 (Zhurong rover) showing on an image mosaic (0.7 m/pixel) covering the main landing region (red polygon) generated from images acquired by the high-resolution imaging camera onboard the Tianwen-1 orbiter. The cyan polygon shows the target landing area in southern Utopia Planitia. The background image is a color shaded relief of the Mars Orbiter Laser Altimeter (Smith et al., 2001) data.

of the common feature points in the X and Y directions as well as their combined error vectors in 2D (Figure S1 in Supporting Information S1). The results revealed a root mean square error (RMSE) of 10.2 and 12.8 m along the X and Y directions, respectively, with an RMSE of 16.4 m for the combined error vectors in 2D. The vertical accuracy of the generated DEM was evaluated by comparison with the MOLA DEM covering the entire main landing region and the meter-resolution DEMs covering partial of the region generated from the MRO High-Resolution Imaging Experiment (HiRISE) images. Four profiles (two along the north-south direction and two along the west-east direction) were extracted from the HiRIC DEM and MOLA DEM, respectively. The elevation differences between the corresponding profiles were calculated. A mean absolute difference of 12–18 m and a maximum absolute difference of approximately 280 m were found (Figure S2 in Supporting Information S1). The maximum elevation difference was found inside a large crater close to the southwest boundary of the main landing region, in which the profile of the MOLA DEM was 280 m shallower than that of the HiRIC DEM. This difference could be attributed to the possible missing measurements of the crater floor from MOLA (the HiRIC DEM fully reconstructed the topographic details of the crater). The two HiRISE DEMs generated by the HiRISE team (available from https://www.uahirise.org/dtm/ESP_069665_2055 and ESP_069876_2055) covering the Zhurong landing site and its neighboring region were used for comparison with the HiRIC DEM to evaluate the fine-scale accuracy and topographic details. The two HiRISE DEMs both have a spatial resolution of 1 m/pixel, and they were merged into one for comparison with the HiRIC DEM in their overlapping region (Figure S3 in Supporting Information S1). Visual comparison of the color-shaded DEMs shows that the HiRISE DEM preserves finer topographic details than the HiRIC DEM, as the former has a better spatial resolution of 1 m/pixel than 5 m/pixel of the latter. Two profiles were extracted from the HiRISE and HiRIC DEMs, respectively. The elevation profiles derived from the two DEMs were in general consistent as shown in Figure S3 in Supporting Information S1, with a mean absolute elevation difference of 1.32–5.1 m.

Based on the 5 m/pixel DEM, surface slopes were calculated and analyzed at a baseline of 10 m, which is approximately the size of the lander footprint plus a buffer space for maneuvering during touch down. Slopes are the gradients of elevations calculated at a specific baseline. For any point in the DEM, its eight neighbors are used to

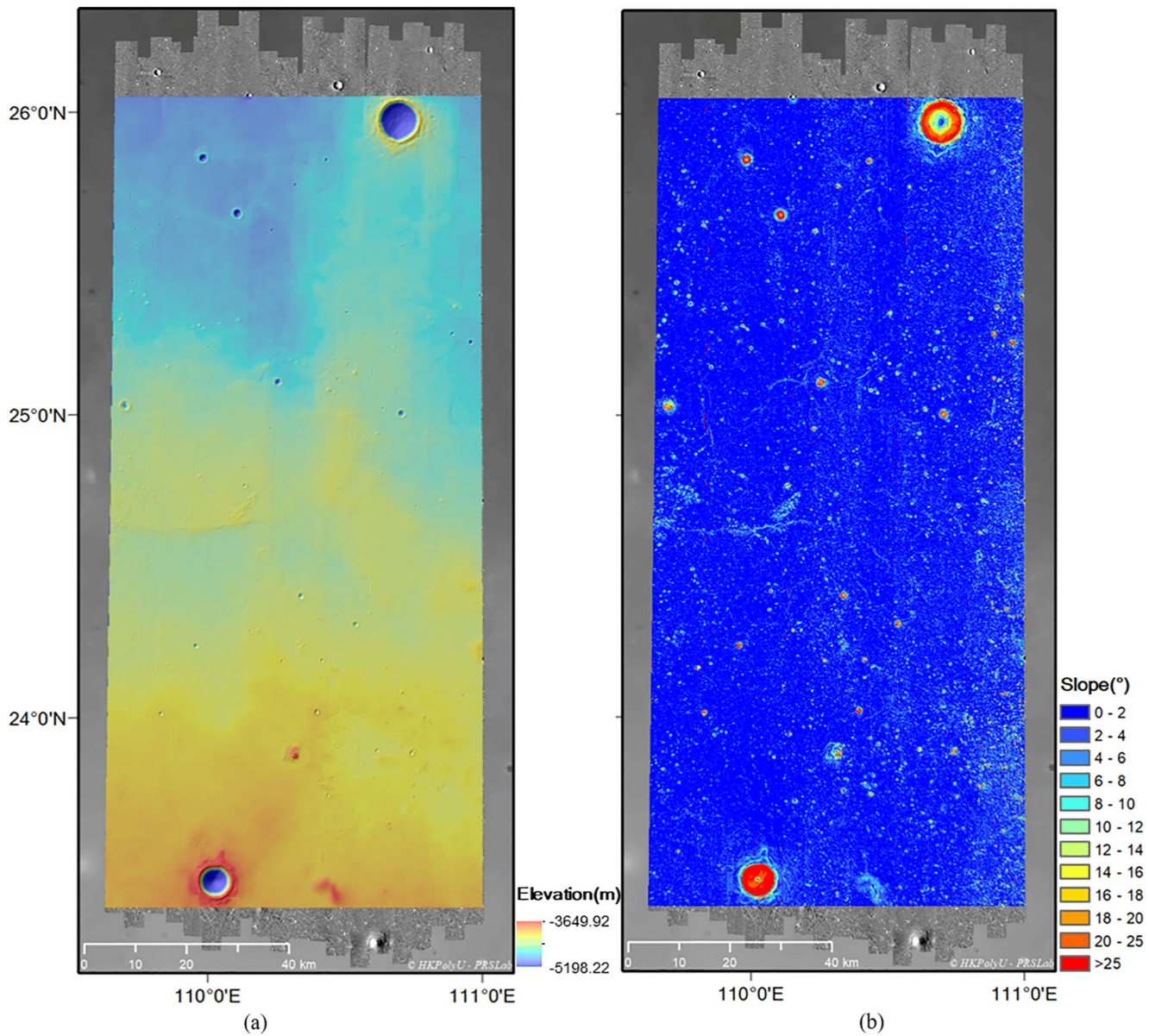


Figure 2. (a) Generated digital elevation model (DEM) (5 m/pixel) from stereo high-resolution imaging camera images covering the main landing region (the red polygon in Figure 1); and (b) slope map (5 m/pixel) at a 10 m baseline derived from the DEM.

calculate the slopes along the North-South and East-West directions based on their weighted distances and elevation differences; the square root of the sum of their squares is determined as the slope at that point (Horn, 1981). The calculated slope values were sampled every 5 m to generate a slope map covering the main landing region, as shown in Figure 2b. The average slope was 2.1°, the maximum slope was 63.0° and the standard deviation was 3.3°. The majority (96.4%) of the main landing region had surface slopes less than 8° (engineering threshold for selecting a flat landing site; Wu et al., 2021). Large slopes were mainly distributed around craters, cones, troughs and ridges. Detailed slope distributions and histogram can be found in Figure S4 in Supporting Information S1. The slope distribution at Zhurong's main landing region was compared with the slopes at the InSight landing region (Golombek, Kass, et al., 2020) as their terrain surfaces appeared to be similar. A DEM generated from a pair of CTX images covering the InSight landing site (Ferguson et al., 2016) was downloaded (https://astrogeology.usgs.gov/search/map/Mars/InSight/landing_site/D18_034150_1838_D17_033728_1838_20m_DTM_destripe) for analysis, from which slopes at a baseline of 20 m were calculated. The slopes at the InSight landing region had an average slope of 4.4° and a maximum slope of 73.5°, slightly greater than those in Zhurong's main

landing region. For slopes less than 8° , the InSight landing region had a percentage of 89%, less than the 96.4% in Zhurong's main landing region; however, the former had relatively unified percentages for each slope range at a 2° interval, but the latter had majority of the slopes (71.62%) distributed within the slope range of 0° – 2° . This indicated that Zhurong's main landing region had relatively smoother terrain surfaces than the InSight landing region.

2.2. Crater Detection and Density Analysis

Craters are possible hazards in landing site evaluation owing to their internal slopes and protuberant rims (Brady et al., 2009; Pajola et al., 2016), especially for small and young craters. Terrain surfaces with high crater densities will reduce the flexibility in hazard avoidance during the descent phase of the lander and limit the maneuvering capability of the rover during surface operations (Wu et al., 2014, 2021).

The HiRIC image mosaic (0.7 m/pixel) covering the main landing region was used for automatic crater detection based on an active machine-learning approach (Wang & Wu, 2019). The approach has a detection rate of approximately 85% for craters covering 20 or more pixels on the images, with the detection rate decreasing for smaller craters. Therefore, we used this approach to detect craters with diameters of ≥ 14 m based on the HiRIC image mosaic to ensure the best automatic detection performance. Manual checking was further conducted to ensure the accuracy and completeness of the final detected craters. Finally, 670,778 craters with diameters ranging from 14 m to 8,125 m were detected in the main landing region. Examples of the crater detection results are shown in Figure 3.

Based on the crater detection results, crater density values were calculated by determining the percentage of area covered by craters (≥ 14 m in diameter) within a moving circular window of radius 1 km. The crater density values were sampled every 5 m to generate a crater density map covering the main landing region (Figure 3a). The crater density map revealed that craters were concentrated in local regions, such as in the southern and north-western areas of the main landing region. The central-northern part had lower crater densities. The average crater density was approximately 10%, with a standard deviation of 8.2%. The maximum crater density was 100%, which occurred inside the two large craters close to the northern and southern boundaries of the main landing region.

2.3. Rock Extraction and Abundance Analysis

Rocks are another type of major feature on the Martian surface that can be hazardous for the lander and rover. Rock abundance, a measure of the cumulative fractional area covered by rocks with respect to the rock diameter, is a critical factor for landing site evaluation (Golombek & Rapp, 1997; Golombek et al., 2012; Pajola et al., 2017; Wu et al., 2018, 2021). Golombek and Rapp (1997) presented an exponential function of the rock abundance model based on rock measurements at the two Viking landing sites, which has been widely used to represent rock abundance on the Martian surface because it favorably matches the rock size–frequency distribution curves with real measurements taken from ground images at different landing sites (Golombek et al., 2003, 2012). A constraint on rock abundance in landing site selection is related to the ability to tolerate rocks of the lander and rover during their maneuvering. Considering the rover traverse performance and the probability of encountering a rock hazard during landing, a threshold of rock abundance should be considered in landing site selection. For instance, a rock abundance constraint of less than 10% was applied for selecting the InSight landing site (Golombek et al., 2017).

The HiRIC image mosaic (0.7 m/pixel) covering the main landing region was used for automatic rock extraction based on a deep-learning approach (Bochkovskiy et al., 2020). The deep-learning approach can achieve a rock detection rate of approximately 70%–80%, as evaluated by comparing the rock extraction results from deep learning and manual digitization at several testing sites. Extensive manual checking processes were further conducted by a group of independent operators to exclude false detections and add omitted rocks, which improved the rock detection rate to approximately 85%. Finally, over 2 million rocks with diameters ranging from 1.4 to 8 m were extracted from the HiRIC image mosaic in the main landing region. Figure 4 shows examples of the rock extraction results. Given the extremely large number of rocks, it is possible that the results might have missed rocks or included false positives. However, because we evaluated rock abundances in local areas relative to other areas within the main landing region, a small percentage of missed rocks or false positives was considered acceptable because this situation was generally consistent throughout the main landing region. It should also be noted that there are some artifacts in the rock abundance map, mainly due to the vertical striping from the mosaic of HiRIC

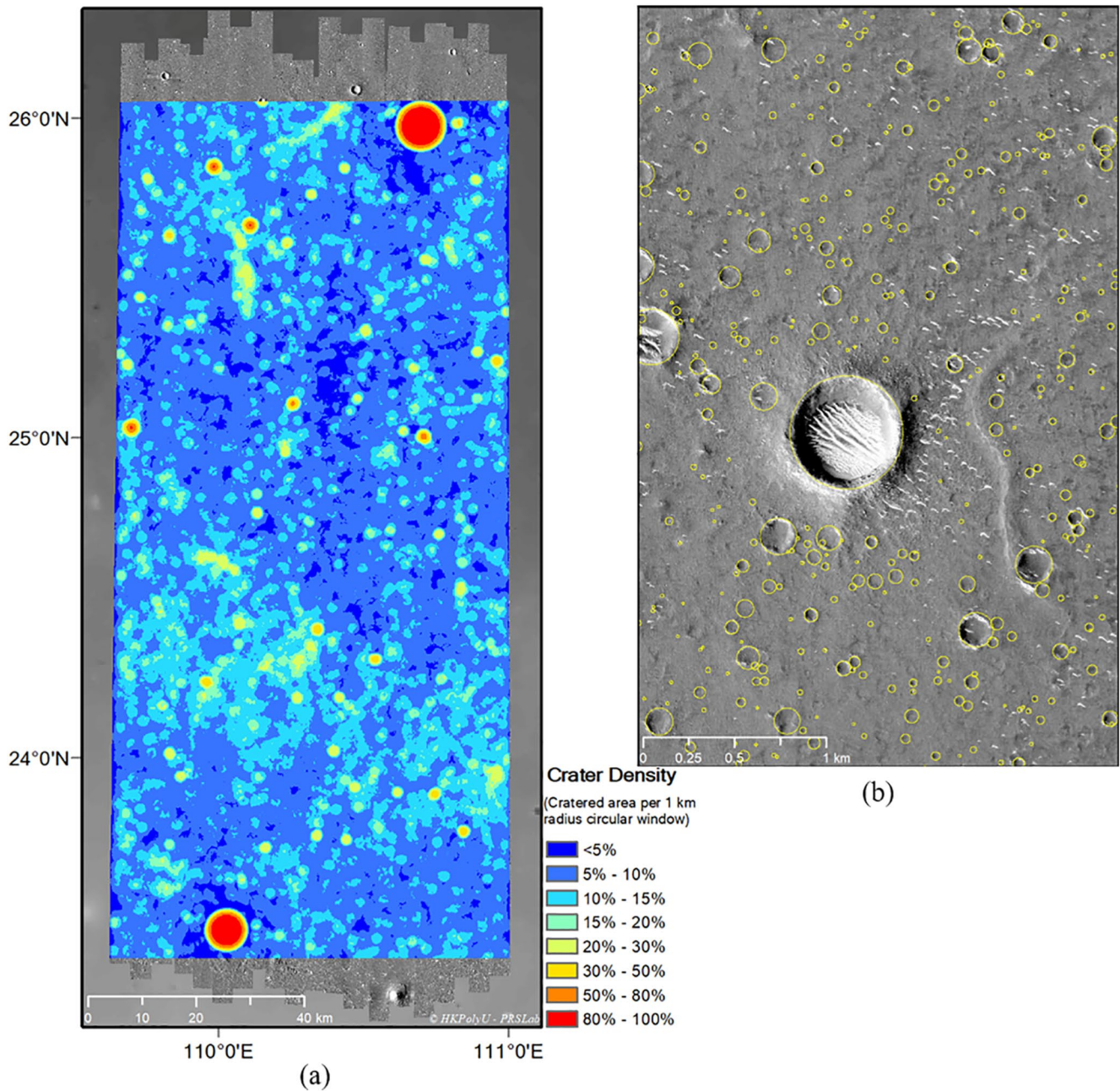


Figure 3. (a) Crater density map (5 m/pixel) of the main landing region (the red polygon in Figure 1); and (b) enlarged view showing examples of detected craters on a high-resolution imaging camera image around the center of the main landing region.

images and the illumination differences between different orbits of HiRIC images. These artifacts are considered understandable given the challenge of creating such a mosaic.

The extracted rocks were then used to estimate the rock abundance values by fitting the cumulative size-frequency distribution of rocks in a moving circular window (of radius 250 m) to the rock abundance model (Golombek & Rapp, 1997). The rock abundance values were sampled every 5 m to generate a rock abundance map covering the main landing region, as shown in Figure 4a. It shows that the southern and north-eastern parts of the main landing region had higher rock abundances. The central-western and north-western parts had lower rock abundances (Figure 4a). The average rock abundance within the main landing region was 8.7%, with a standard deviation

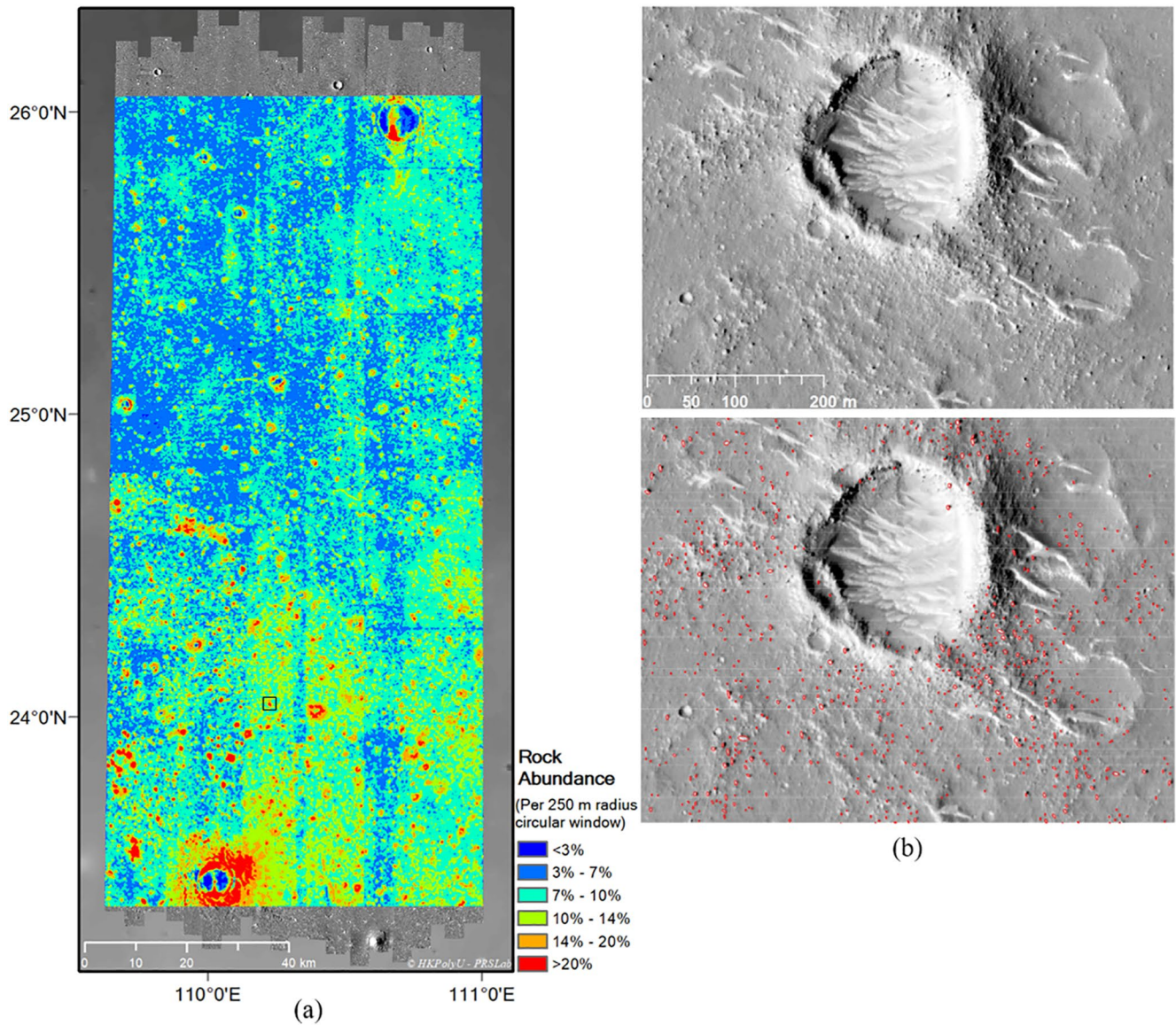


Figure 4. (a) Rock abundance map (5 m/pixel) of the main landing region (the red polygon in Figure 1); and (b) examples of detected rocks (red ellipses) in a high-resolution imaging camera image of a representative local region as marked by the black box in panel (a).

of 3.2%. The maximum rock abundance was 57%, which occurred around the large crater close to the southern boundary of the region.

2.4. Landing Ellipse Search

Based on the generated slope map, crater density map and rock abundance map, a hazard index map was derived for the main landing region. For each pixel i on the map, its hazard index H is defined as follows:

$$H = W_s \times \frac{S_i}{\bar{S}} + W_R \times \frac{R_i}{\bar{R}} + W_C \times \frac{C_i}{\bar{C}} \quad (1)$$

where S_i is the slope value of pixel i and \bar{S} is the normalized slope of 8°. R_i is the rock abundance value of pixel i and \bar{R} is the normalized rock abundance of 10%. C_i is the crater density value of pixel i and \bar{C} is the normalized crater density of 10%. The normalized slope, rock abundance, and crater density values were used as references for determining the presence of a potential hazard based on engineering constraints considering the capabilities

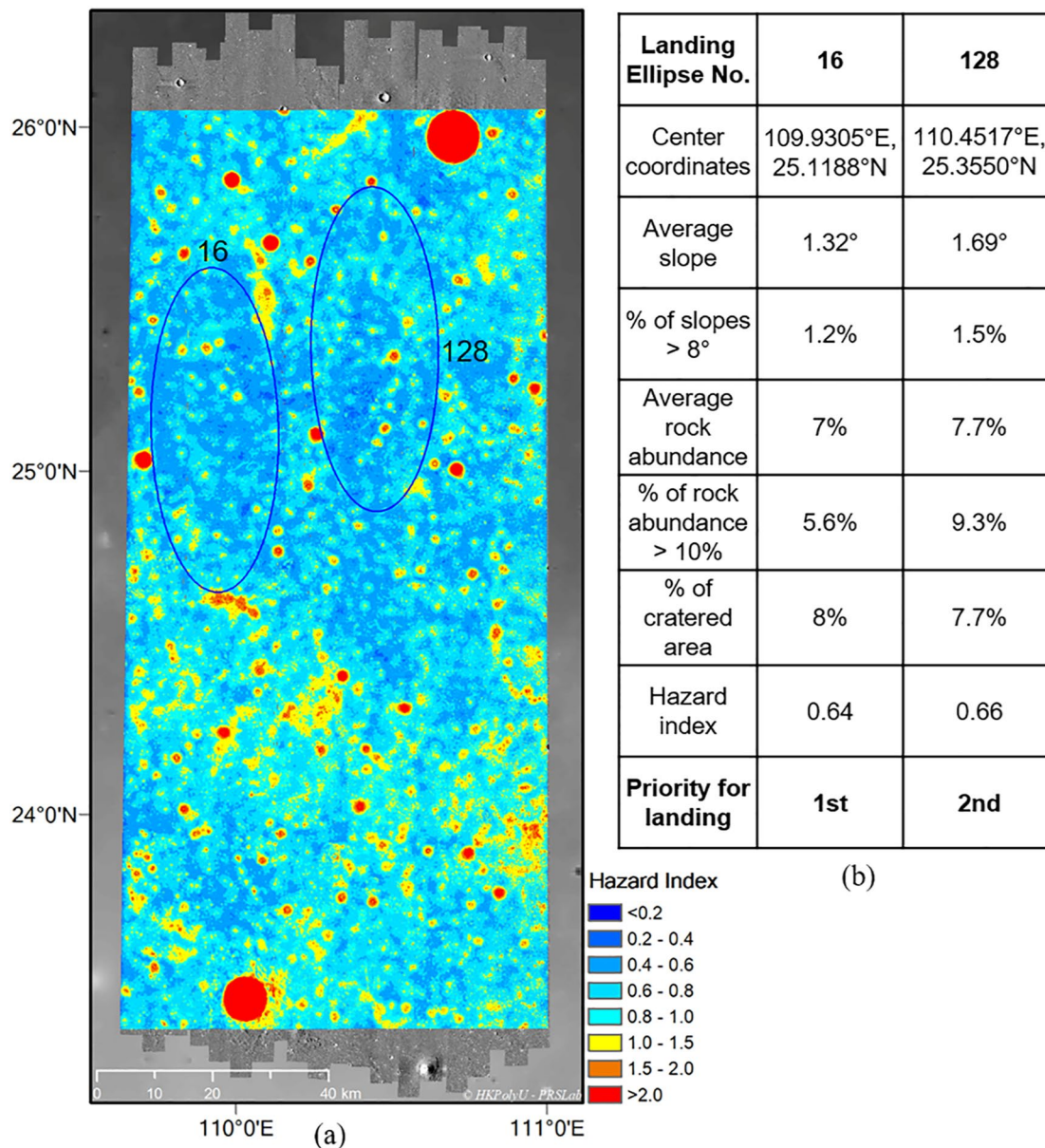


Figure 5. (a) Hazard index map (5 m/pixel) of the main landing region (the red polygon in Figure 1) and the shortlisted landing ellipses; and (b) parameters of the shortlisted landing ellipses.

of the lander and rover to tolerate potential hazards during touchdown and surface operations (Dong et al., 2019; Wu et al., 2021). W_s , W_R , and W_C are the weights of the slopes, rock abundances and crater densities, respectively, which control their contributions to the hazard index. A weight of 0.3 was used for both W_s and W_R , whereas a higher weight of 0.4 was used for W_C because compared with potential hazards caused by slopes or rocks, we considered craters more dangerous. Areas with high crater densities will lead to reduced flexibility of hazard avoidance during the descent phase of the lander. Moreover, the lander should avoid landing in any small craters to allow for the maximum maneuvering capability of the rover.

From the calculated hazard index at each pixel based on the maps of slopes, crater densities and rock abundances, a hazard index map with the same resolution of 5 m/pixel was generated covering the main landing region, as shown in Figure 5a. The hazard index map combines the influences of slopes, crater densities and rock abundances. Overall, the southern part of the main landing region had higher hazard index values (red and yellow). The central-western and north-western parts of the region had lower hazard index values (dark blue).

Based on the foregoing results, further searching for landing ellipses was conducted. The dimensions of the landing ellipse (Figure 5a) are 56 km along the major axis and 22 km along the minor axis, defined as 3σ of uncertainty for landing. The major axis of the landing ellipse has a tilted angle of 1.35° from the north toward the west, defined based on the descent orbit design.

The following criteria were applied when searching for landing ellipses within the main landing region: (a) the percentage of areas with slopes $>8^\circ$ within the ellipse should be less than 10%; (b) the percentage of areas with rock abundances $>10\%$ within the ellipse should be less than 10%; and (c) the percentage of areas covered by craters within the ellipse should be less than 10%. An automatic software was developed for iterative searching of landing ellipses that fulfilled the above criteria within the main landing region. The search pace was set as 2 km between any two landing ellipses.

One hundred and thirty-seven landing ellipses were found using the iterative search process. Their average hazard index values were then calculated, and the landing ellipses were ranked based on the hazard index. For landing ellipses with similar hazard index values, other detailed parameters (e.g., average slope, percentage of areas with slopes $>8^\circ$, average rock abundance, percentage of areas with rock abundances $>10\%$, and percentage of areas covered by craters within the ellipse) were considered for further ranking. For local regions with many clustered ellipses, only the best one was selected.

Finally, two landing ellipses (Nos. 16 and 128) were shortlisted owing to their superiority in the aforementioned factors. As shown in Figure 5a, the distributions of the two shortlisted landing ellipses generally matched the areas with low hazard index values (dark blue) within the main landing region. Among the two landing ellipses, No. 16 had the lowest hazard index among all of the searched landing ellipses and was superior to No. 128 for most of the parameters, as shown in Figure 5b. Therefore, No. 16 was selected as the landing ellipse of the first priority, which is where the Zhurong rover eventually landed.

3. Landing Site Characterization

3.1. Landing Site Location and Geomorphological Features of Scientific Interest

On 15 May 2021, the Tianwen-1 lander carrying the Zhurong rover successfully landed near the center of ellipse No. 16 in the main landing region (Figure 6a). On 2 June 2021, the HiRIC onboard the Tianwen-1 orbiter re-visited the landing site and collected a high-resolution image (0.7 m/pixel) of the region after landing. Figure 6b shows an enlarged view of the landing site and its nearby region. The locations of the lander, parachute and back cover, and heat shield jettisoned during the descent phase are recognizable in Figure 6b. The actual location of the lander was 109.925°E , 25.066°N at an elevation of $-4,099.4$ m in the MOLA DEM, approximately 3.1 km south of the center of ellipse No. 16.

Figure 6a shows that the landing site is generally flat and smooth. More than 10 pitted cones with sizes of several hundred meters are distributed to the north. Clusters of pitted cones of smaller sizes are also distributed to the south. These pitted cones are important windows to help understand the geological history of the region. There are several hypotheses on the origin of these pitted cones. One is rootless cones formed by explosive interactions between surficial lavas and near-surface groundwater (Bruno et al., 2006; Xiao & Wang, 2009). Another is mud volcanism (Ye et al., 2021), a process on Earth that is usually associated with methane release (Farrand et al., 2005; Oehler & Allen, 2010). Other hypotheses include terrestrial Maars (White & Ross, 2011) and pingos (MacKay, 1998). The exact origin of these pitted cones in the landing region requires further investigation. However, all of the hypotheses are related to water/ice or volatiles (McGowan & McGill, 2007).

Figure 6 also shows craters of various sizes distributed around the landing site. Some of these craters have little relief and are filled with fine-grained material. Some craters have bright and sharp rims and ejecta indicating that they are relatively new. Several troughs cross the western and eastern regions of the landing site (Figure 6a). They have widths of approximately 200–300 m and depths of approximately 4–6 m. Hypotheses on the origin of these troughs include tectonic extension of the Utopia basin (Zhao et al., 2021) following the sublimation of a body of ice in the depression (Hiesinger & Head, 2000) or volumetric compaction (Cooke et al., 2011).

There are many light-toned barchan bedforms recognizable in Figure 6b, indicating aeolian processes over the landing region. The aeolian bedforms on the surface are typically dozens of meters in length and approximately

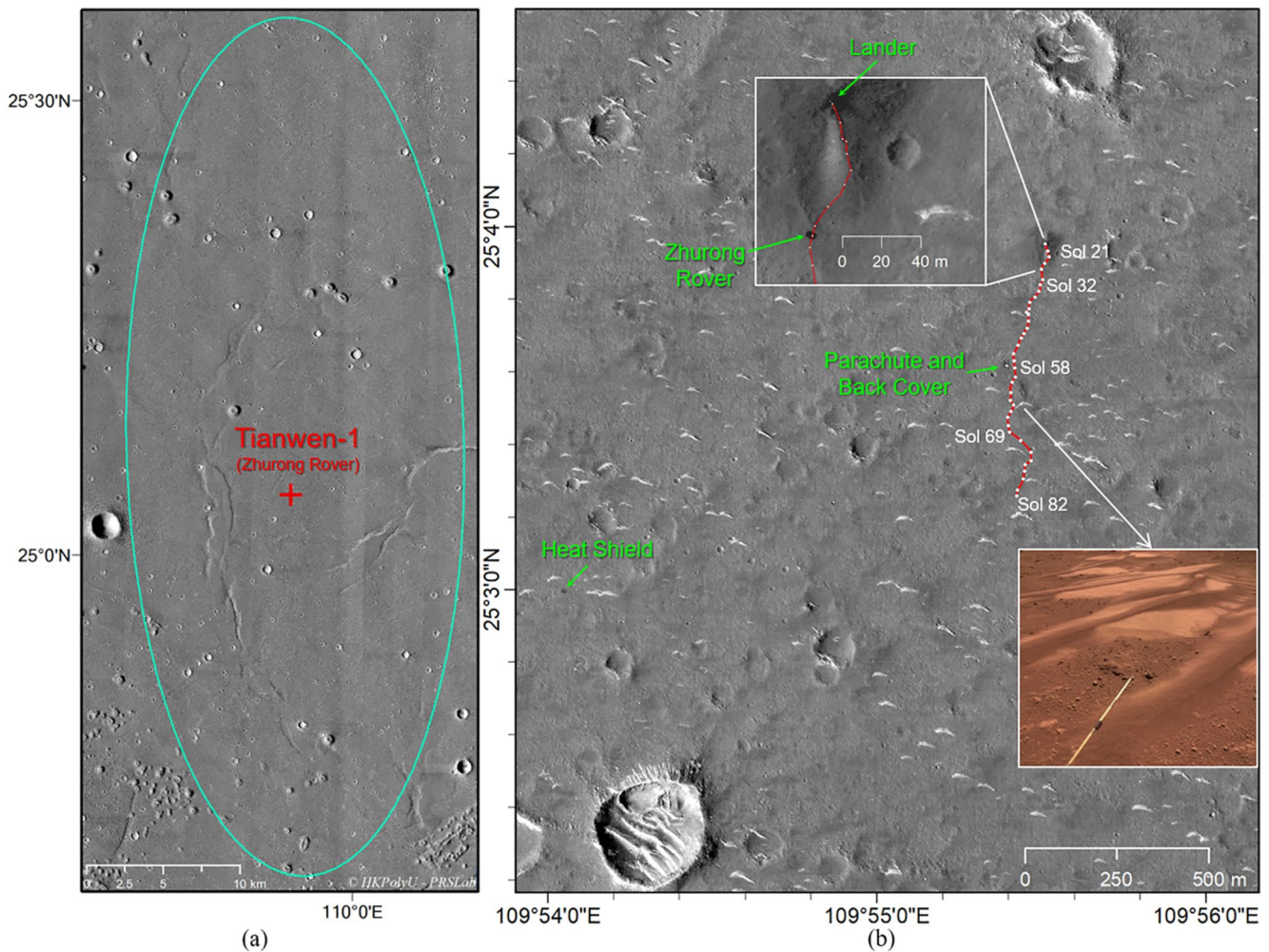


Figure 6. (a) Tianwen-1 (Zhurong rover) landing site shown in the high-resolution imaging camera (HiRIC) image mosaic with ellipse No. 16 marked in cyan; and (b) enlarged view of the landing site shown in the HiRIC image (HX1-Or_GRAS_HiRIC-CCD1-F_SCI_N_20210602133202) showing the locations of the lander (109.925°E and 25.066°N), the parachute and back cover (109.901°E and 25.050°N), the heat shield (109.901°E and 25.050°N), and the traverse (red) and locations (white dots) of the Zhurong rover up to Sol 82. The upper inset shows an enlarged view of the locations of the lander and the Zhurong rover. The lower inset shows an example of the aeolian bedform on an image (HX1-Ro_GRAS_NaTeCamA-F-004_SCI_N_20210718125903) taken by the NaTeCam onboard the Zhurong rover on Sol 62. The white steak on the image is an antenna of the penetrating radar onboard the Zhurong rover.

0.5 m in height. The main directions of the aeolian bedforms are from northwest to southeast, which indicates a similar prevailing wind direction in the region (Sefton-Nash et al., 2014; Zhao et al., 2021).

As of 6 August 2021 (Sol 82), the Zhurong rover has traveled 808 m to the south of the lander (Figure 6b), visited the location of the parachute and back cover at Sol 58, and explored features of scientific interest over the region. In situ investigation by the Zhurong rover could provide a detailed study of these features.

3.2. Surface and Shallow Subsurface Properties

Figure 7a shows a ground panorama of the landing site captured by the NaTeCam onboard the Zhurong rover before it was released from the lander to the ground. The surface of the landing site and its nearby region is smooth, with a few rocks. The resolvable particle size distribution from the lander is dominated by granules, pebbles, and cobbles. They have shapes of mainly sub-equant and angular and sizes ranging from several millimeters to several decimeters in diameter. A bedrock of approximately 3.2 m in length is present approximately 10 m north of the lander. Many of the rocks close to the lander have a bright gray color; several dark-toned rocks are also present. Some of the rocks are clearly fluted, suggesting aeolian abrasion.

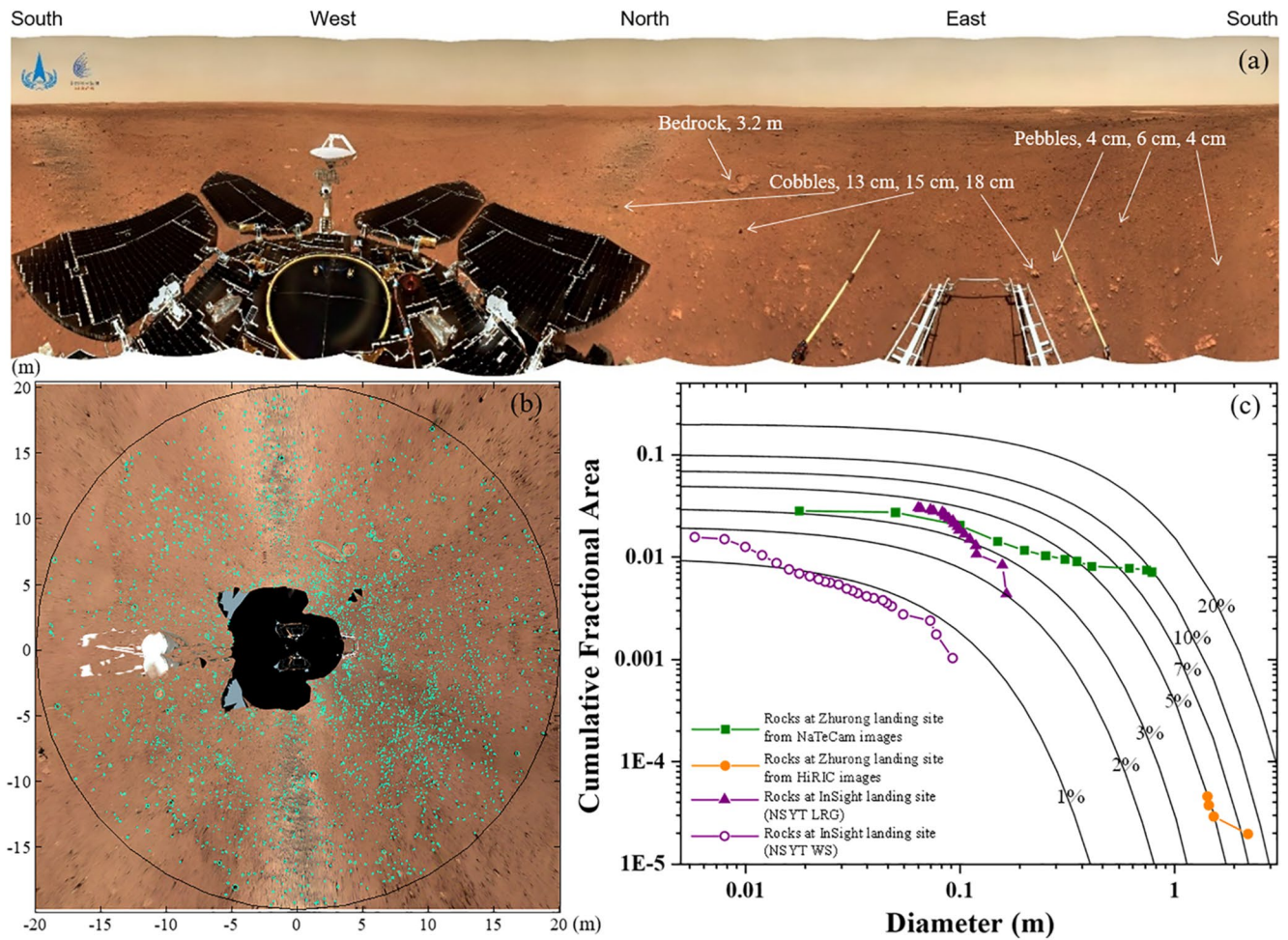


Figure 7. (a) Ground panorama of the landing site captured by the NaTeCam onboard the Zhurong rover before it was released from the lander; (b) extracted rocks from an ortho-rectified image mosaic generated from the NaTeCam images; and (c) cumulative fractional area covered by rocks versus rock diameter at the Zhurong landing site measured from NaTeCam images (green, rock abundance of $\sim 4\%$) and high-resolution imaging camera orbital images (brown, rock abundance of $\sim 5\%$), and at the InSight landing site in local regions of the workspace (NSYT WS; purple with circles, rock abundance of $\sim 1\%$) and the area to the south with large rocks (NSYT LRG; purple with triangles, rock abundance of $\sim 4\%$). The rock data at the InSight landing site are from Golombek, Kass, et al. (2020). The black lines are modeled rock abundance of 1%, 2%, 3%, 5%, 7%, 10%, and 20% for reference.

Figure 7b shows an ortho-rectified image mosaic generated from the NaTeCam images, on which rocks manually delimited are shown within a circular range (40 m in diameter) centered at the lander. Figure 7c shows a chart of the cumulative fractional area covered by rocks versus rock diameter. The green line shows the rock distribution at the Zhurong landing site as measured from the NaTeCam images, indicating a rock abundance of approximately 4% based on the rock abundance model (Golombek & Rapp, 1997). Rocks measured from the HiRIC orbital images within the same area are plotted in brown, which shows a good agreement with the surface measurements at a slightly higher rock abundance of approximately 5%. Rock distributions at the InSight landing site (Golombek, Kass, et al., 2020) are also plotted in Figure 7c for comparison, which include a local region of the workspace (NSYT WS) (purple with circles) and a local area to the south with large rocks (NSYT LRG) (purple with triangles). They indicate rock abundances of 1%–4% at the InSight landing site, slightly lower than the rock abundance of $\sim 4\%$ at the Zhurong landing site. The Spirit landing site also has a rock abundance of 4% (Golombek et al., 2003), similar to the Zhurong landing site. These landing sites represent the most granule- to pebble-rich landing sites on Mars, which may be due to deflation where finer particles have been removed by wind.

During touchdown, the pulsed retrorockets disturbed the surface and excavated a hole beneath the lander (Figure 8), thereby offering a unique opportunity to study the structure of the shallow regolith below the surface

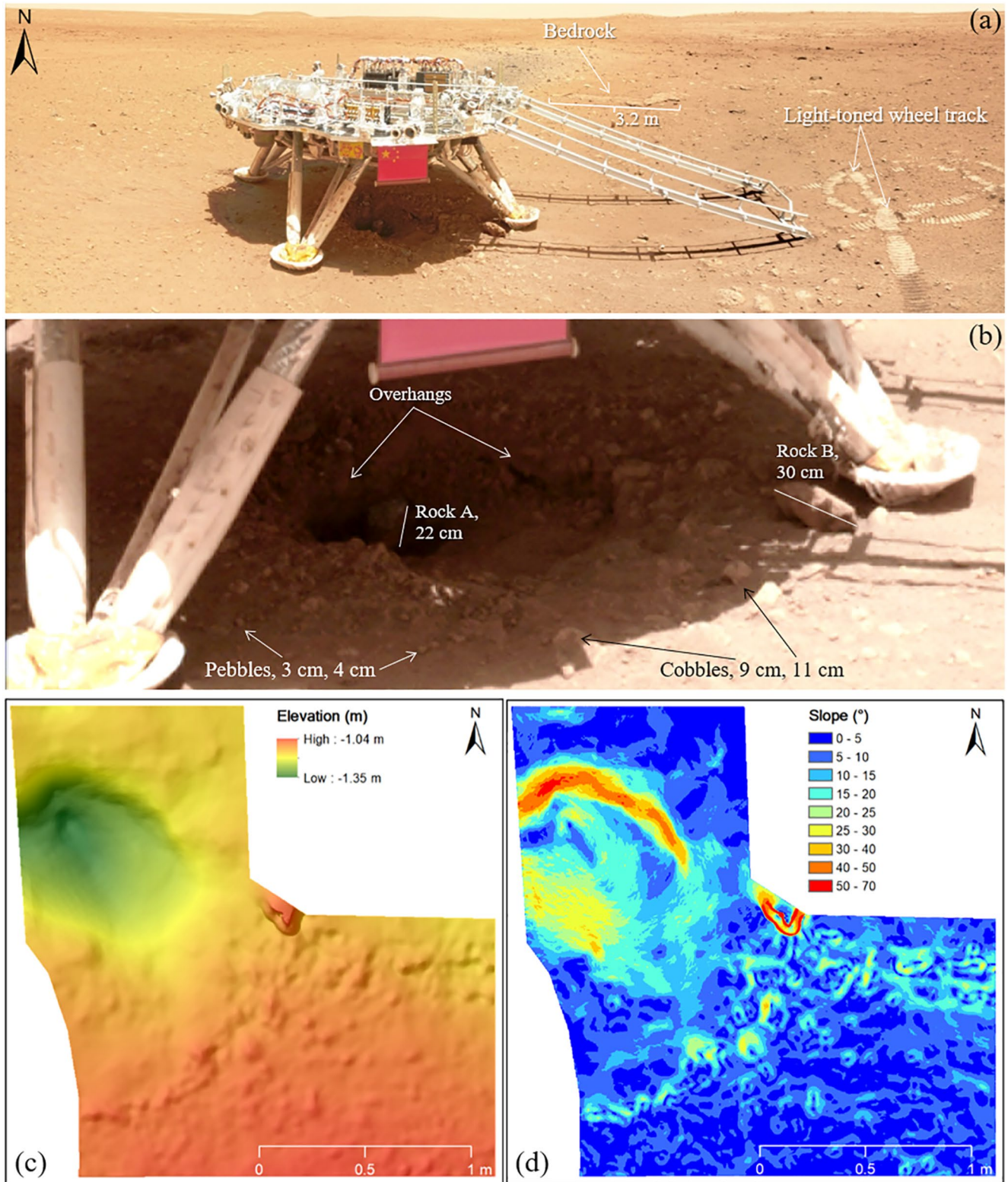


Figure 8. (a) An image of the lander captured by the Navigation and Terrain Camera (NaTeCam) from a distance of approximately 5 m, showing a hole beneath the lander excavated by the retrorockets during touchdown; (b) enlarged view of the hole showing various features; (c) a digital elevation model (DEM) of the hole and the nearby terrain surface generated from photogrammetric processing of stereo pairs of NaTeCam images; and (d) a slope map derived from the DEM.

and their physical properties. Figure 8a shows the wheel tracks of the Zhurong rover on the ground after it was released from the lander. The wheel tracks show bright patterns of fine sand and dust, indicating that the topmost surface materials are composed of sand and fines (Sullivan et al., 2011).

The NaTeCam onboard the Zhurong rover acquired several pairs of stereo images of the lander and the hole from a distance of approximately 5 m, and these images were processed using our in-house photogrammetric software (Hu & Wu, 2019) to generate a DEM covering the hole and the nearby terrain surface as shown in Figure 8c. The DEM has a spatial resolution of 3 mm/pixel and is in a local coordinate system with the origin at the center of the lander's platform. A slope map was also derived based on the DEM as shown in Figure 8d. As revealed from the DEM, the hole is elliptical with a major axis of 0.95 m and a minor axis of 0.7 m. Its depth is at least 0.3 m (visible part on the NaTeCam images). In and around the hole (see in Figure 8b), the exposed subsurface material is poorly sorted, with pebbles and cobbles generally of centimeter size. Smaller clods are scattered over the region beneath the lander. There are two larger rocks noticeable. Rock A is inside the hole with a size of approximately 22 cm leaning on the wall. Rock B is adjacent to one of the footpads of the lander in the east with a size of approximately 30 cm, which might have been excavated by the pulsed retrorockets. The southern wall of the hole has moderate slopes of approximately 15°–30°. The northern wall of the hole has steep slopes (up to 70°) with resistant layers, vertical edges and overhangs. Some of the layers have pebbles and cobbles that appear cemented in fine-grained materials. These layers show internal strength to steep slopes and seem to be mechanically strong, similar to duricrust formed as a result of cementation via interaction between water and unindurated soils as those seen on Earth (Conacher, 1991) and Mars (Haskin et al., 2005).

During the landing of the InSight spacecraft, its pulsed retrorockets also modified the surface and revealed a near surface stratigraphy of surficial dust, over thin unconsolidated sand, underlain by a variable thickness duricrust, with poorly sorted, unconsolidated sand with rocks beneath (Golombek, Warner, et al., 2020). The surface and subsurface materials from thruster excavation at the Zhurong and InSight landing sites seem similar, indicating a similar shallow subsurface structure of the two landing sites.

The above observations suggest that the Zhurong landing site has a shallow regolith structure of a surficial layer of dust and sand over a layer of duricrust, with brecciated/fragmented rocks and bedrocks beneath. This is consistent with the Thermal Emission Spectrometer orbital measurements of thermal inertia and albedo values at the Zhurong landing site (thermal inertia: $258 \text{ Jm}^{-2}\text{s}^{-0.5} \text{ K}^{-1}$; albedo: 0.23), which indicate a “C type” surface property of duricrust, some sand, rocks and bedrock (Putzig et al., 2005).

3.3. Surface Age of the Landing Region

The landing area of Tianwen-1 (Zhurong rover) was mapped as a Late Hesperian lowland (IHL) unit (Tanaka et al., 2014) with an estimated age of 3.34 Ga (Wu et al., 2021). Previous studies have indicated that the IHL unit is mainly composed of Vastitas Borealis Formation (VBF) materials, which might have originated from fluvial, lacustrine or marine sediments (Carr & Head, 2019; Ivanov & Hiesinger, 2020; Kreslavsky & Head, 2002). However, significant uncertainty remains regarding the geological history and origin of the lowland unit in southern Utopia Planitia.

To examine the surface age of the local region where Zhurong landed, crater size-frequency distribution (CSFD) analysis was conducted using craters of smaller sizes (≥ 80 m) detected in the HiRIC images within the main landing region (Figure 9a). Possible secondary craters were excluded manually based on clues such as their distribution and visual distinctness from primary craters (Robbins & Hynek, 2014; Wu et al., 2020). Figure 9b shows the crater size-frequency plot. A noticeable gap occurred in the plot between crater diameters of approximately 500 and 800 m. Thus, the age estimation for the main landing region was divided into two parts using craters with diameters from 80 to 500 m and greater than 800 m, respectively. Craters ≥ 800 m were used for comparison with the age estimation in the entire IHL unit (which also used craters ≥ 800 m (Wu et al., 2021)). It shows an age of $3.01^{+0.23}_{-0.47}$ Ga, which is in general agreement with the age of 3.34 Ga for the entire IHL unit. However, the age obtained using smaller craters (80–500 m) with a resurfacing correction in Craterstates (Michael & Neukum, 2010) is much younger at $1.12^{+0.01}_{-0.01}$ Ga. The crater counting area has a size of approximately 12,000 km², which is considered statistically sufficient according to Warner et al. (2015). Therefore, the younger age derived from small craters may indicate a possible local emplacement or resurfacing event around the landing region in

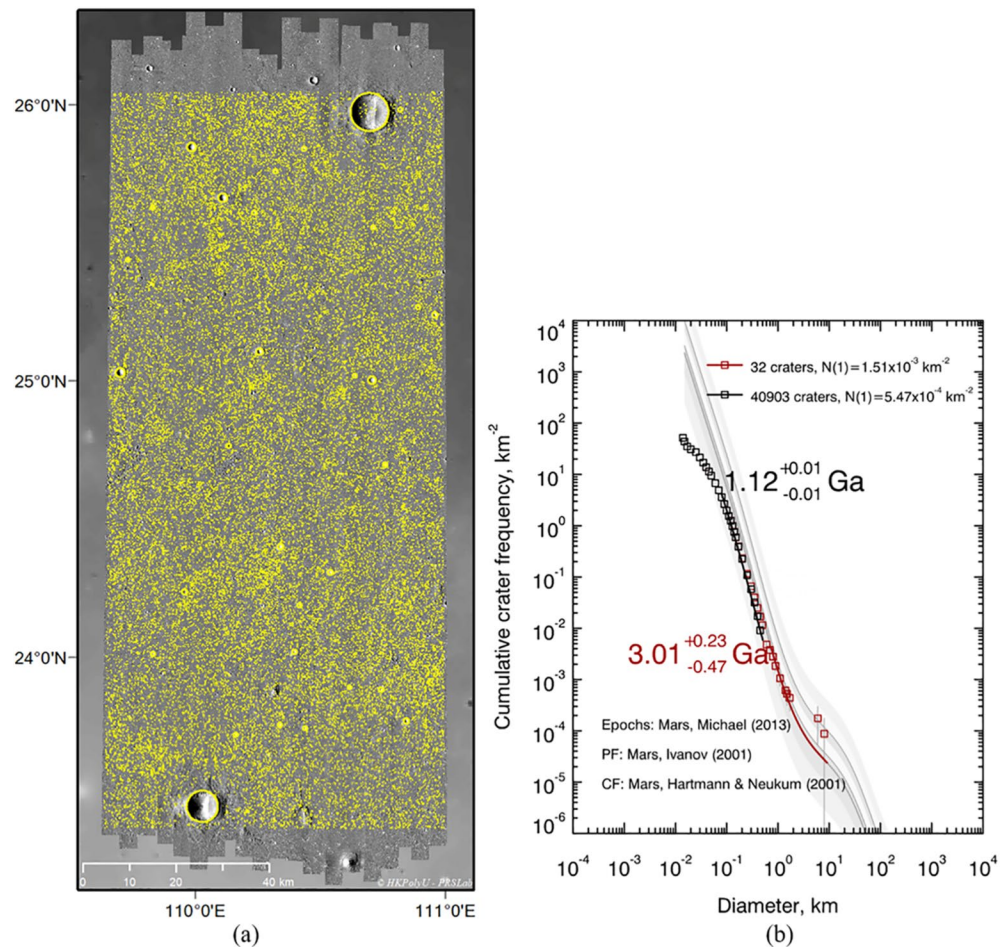


Figure 9. (a) Craters used for detailed crater size-frequency distribution analysis within the main landing region; and (b) crater size-frequency plots and estimated ages using craters ≥ 800 m in diameter (red) and craters of diameter ranges from 80 to 500 m with a resurfacing correction (black).

the middle Amazonian. However, what exactly is the emplacement or resurfacing event requires further investigation in terms of the geologic and geomorphological characteristics of the region on a larger scale.

4. Conclusions and Discussion

This paper presents our efforts in the last stage of landing site searching and selection for Tianwen-1 (Zhurong rover) within a pre-identified main landing region in southern Utopia Planitia. The joint analysis of surface slopes, crater densities and rock abundances enabled the optimized search for landing ellipses with minimum hazards within the main landing region. This process was conducted in approximately two months, from early March to early May 2021, and assisted the successful landing of Tianwen-1 (Zhurong rover) in the selected landing ellipse on 15 May 2021. After landing, the actual landing site was localized and features of scientific interest in the nearby region were examined. Surface images captured by the NaTeCam onboard the Zhurong rover revealed a low rock abundance of approximately 4% at the landing site, similar to the rock measurements from orbital data before landing. Surface and subsurface images suggested a shallow regolith structure of a surficial layer of dust and sand over a layer of duricrust, with brecciated/fragmented rocks and bedrocks beneath. The CSFD analysis indicated that multiple episodes of resurfacing might have occurred in the region, including the formation of VBF materials in the late Hesperian (approximately 3.4 Ga) and a local emplacement or resurfacing event around the landing region occurring in the middle Amazonian (approximately 1.12 Ga).

The Zhurong rover will continue to travel to the south of the lander and investigate geomorphological and geologic features of scientific interest. In situ investigation by the Zhurong rover could provide a detailed study of these features, thereby offering further information on the origin of the features, the geological history of the region, and possible subsurface water or ice distribution. Several instruments onboard the Zhurong rover will be particularly useful to further verify the previously described observations. The MSCam can acquire visible-near infrared spectral data of less dusty rocks and soil, which will be helpful to identify sedimentary and igneous rocks over the landing region. The MarSCoDe includes a Laser-Induced Breakdown Spectrometer (LIBS; 240–850 nm), and a short-wave infrared (SWIR) spectrum microscopic imager (850–2,400 nm) (Li et al., 2021). The LIBS can remove the dust or coating on rocks to determine the original rock composition. The LIBS and SWIR abilities of the MarSCoDe will enable detailed analysis of mineralogy and classification of rock types, particle size and compositions, and analysis of water contents of soil or minerals (Maurice et al., 2012). In situ observations from the MSCam and the MarSCoDe will help to verify the combination of VBF sedimentary materials and lava as well as pyroclastic deposits over the landing region.

The RoPeR onboard the rover can characterize the subsurface layer distribution. Its high-frequency channel (0.45–2.15 GHz) can penetrate the subsurface to a depth of 3–10 m with a spatial resolution of several centimeters. Its low-frequency channel (15–95 MHz) can penetrate to a depth of 10–100 m at a spatial resolution of several meters (Zou et al., 2021). The RoPeR can continuously collect underground radar signals along the rover traverse to determine the size and characteristics of the subsurface materials. The RoPeR can investigate the subsurface layered structure in the vertical and horizontal directions, which will be helpful to search for subsurface distribution of possible water ice and volatiles. In situ observations from the RoPeR will verify the aforementioned shallow regolith structure of the land region and further extend to deeper subsurface. The examination of subsurface structure and possible signatures of subsurface water ice from the RoSPR will be of great scientific importance, for example, to confirm the existence of VBF materials (originated from fluvial, lacustrine, or marine sediments) in southern Utopia Planitia, to clarify the origin of the pitted cones over the landing region, and to constrain the geological history of the landing region.

Data Availability Statement

The HiRIC and NaTeCam images are obtained from the Lunar and Planetary Data Release System (<https://moon.bao.ac.cn/web/enmanager/mars1>). The generated datasets at the Zhurong landing site (image mosaics, craters, and rocks) are available at Zenodo (Wu, 2022). The MRO CTX data are available at the Mars Image Explorer (Malin, 2007; <https://viewer.mars.asu.edu/viewer/ctx#T=0>).

Acknowledgments

This work was supported by a grant from the China Academy of Space Technology (Project No: 17CPT/HK0103). This work was also supported by grants from the Research Grants Council of Hong Kong (RIF Project No: R5043-19 and PolyU 15210520). The authors would like to thank all those who worked on the archive of the datasets to make them publicly available.

References

- Bochkovskiy, A., Wang, C. Y., & Liao, H. Y. (2020). *YOLOv4: Optimal Speed and Accuracy of Object Detection*. Computer Vision and Pattern Recognition. Retrieved from <https://arxiv.org/abs/2004.10934>
- Brady, T., Robertson, E., Epp, C., Paschall, S., & Zimpfer, D. (2009). *Hazard Detection Methods for Lunar Landing* (pp. 1–8). Proceedings of the 2009 IEEE Conference on Aerospace.
- Bruno, B. C., Fagents, S. A., Hamilton, C. W., Burr, D. M., & Baloga, S. M. (2006). Identification of volcanic rootless cones, ice mounds, and impact craters on Earth and Mars: Using spatial distribution as a remote sensing tool. *Journal of Geophysical Research*, 111, E6. <https://doi.org/10.1029/2005je002510>
- Carr, M. H., & Head, J. W. (2019). Mars: Formation and fate of a frozen Hesperian ocean. *Icarus*, 319, 433–443. <https://doi.org/10.1016/j.icarus.2018.08.021>
- Conacher, A. J. (1991). Lateritic duricrust and relief inversion in Australia. *Catena*, 18(6), 585–588. [https://doi.org/10.1016/0341-8162\(91\)90041-u](https://doi.org/10.1016/0341-8162(91)90041-u)
- Cooke, M., Islam, F., & McGill, G. (2011). Basement controls on the scale of giant polygons in Utopia Planitia, Mars. *Journal of Geophysical Research*, 116, E9. <https://doi.org/10.1029/2011je003812>
- Dong, J., Sun, Z., Rao, W., Jia, Y., Wang, C., & Chen, B. (2019). Mission profile and design challenges of Mars landing exploration. In B. Wu, K. Di, J. Oberst, & I. Karachetseva (Eds.), *Planetary Remote Sensing and Mapping* (pp. 75–87). Taylor & Francis Group/CRC Press.
- Farrand, W. H., Gaddis, L. R., & Keszthelyi, L. (2005). Pitted cones and domes on Mars: Observations in Acidalia Planitia and Cydonia Mensae using MOC, THEMIS, and TES data. *Journal of Geophysical Research*, 110(E5), E05005. <https://doi.org/10.1029/2004je002297>
- Ferguson, R. L., Kirk, R. L., Cushing, G., Galuszka, D. M., Golombek, M. P., Hare, T. M., et al. (2016). Analysis of local slopes at the InSight landing site on Mars. *Space Science Reviews*, 211(1–4), 1572–9672. <https://doi.org/10.1007/s11214-016-0292-x>
- Golombek, M., Grant, J., Kipp, D., Vasavada, A., Kirk, R., Ferguson, R., et al. (2012). Selection of the Mars Science Laboratory landing site. *Space Science Reviews*, 170, 641–737. https://doi.org/10.1007/978-1-4614-6339-9_18
- Golombek, M., Kass, D., Williams, N., Warner, N., Daubar, I., Piqueux, S., et al. (2020). Assessment of InSight landing site predictions. *Journal of Geophysical Research: Planets*, 125(8), e2020JE006502. <https://doi.org/10.1029/2020je006502>
- Golombek, M., Kipp, D., Warner, N., Daubar, I. J., Ferguson, R., Kirk, R. L., et al. (2017). Selection of the InSight landing site. *Space Science Reviews*, 211(1–4), 5–95. <https://doi.org/10.1007/s11214-016-0321-9>

- Golombek, M., & Rapp, D. (1997). Size-frequency distributions of rocks on Mars and Earth analog sites: Implications for future landed missions. *Journal of Geophysical Research*, 102(E2), 4117–4129. <https://doi.org/10.1029/96je03319>
- Golombek, M., Warner, N. H., Grant, J. A., Hauber, E., Ansari, V., Weitz, C. M., et al. (2020). Geology of the InSight landing site on Mars. *Nature Communications*, 11(1), 1–11.
- Golombek, M. P., Haldemann, A. F. C., Forsberg-Taylor, N. K., Dimaggio, E. N., Schroeder, R. D., Jakosky, B. M., et al. (2003). Rock size-frequency distributions on Mars and implications for Mars Exploration Rover landing safety and operations. *Journal of Geophysical Research*, 108, E12. <https://doi.org/10.1029/2002je002035>
- Haskin, L. A., Wang, A., Jolliff, B. L., McSweeney, H. Y., Clark, B. C., Des Marais, D. J., et al. (2005). Water alteration of rocks and soils from the Spirit rover site, Gusev Crater, Mars. *Nature*, 436(7047), 66–69. <https://doi.org/10.1038/nature03640>
- Hiesinger, H., & Head, J. W., III (2000). Characteristics and origin of polygonal terrain in southern Utopia Planitia, Mars: Results from Mars Orbiter Laser Altimeter and Mars Orbiter Camera data. *Journal of Geophysical Research*, 105, E5. <https://doi.org/10.1029/1999je001193>
- Horn, B. K. P. (1981). Hill shading and the reflectance map. *Proceedings of the IEEE*, 69(1), 14–47. <https://doi.org/10.1109/proc.1981.11918>
- Hu, H., & Wu, B. (2019). Planetary3D: A photogrammetric tool for 3D topographic mapping of planetary bodies. *ISPRS Annals of the Photogrammetry, Remote Sensing and Spatial Information Sciences*, IV-2/W5, 519–526. <https://doi.org/10.5194/isprs-annals-iv-2-w5-519-2019>
- Ivanov, M. A., & Hiesinger, H. (2020). The Acidalia Mensa region on Mars: A key element to test the Mars ocean hypothesis. *Icarus*, 349, 113874. <https://doi.org/10.1016/j.icarus.2020.113874>
- Kreslavsky, M. A., & Head, J. W. (2002). Fate of outflow channel effluents in the northern lowlands of Mars. *Journal of Geophysical Research*, 107(E12), 4–1–4–25. <https://doi.org/10.1029/2001je001831>
- Li, C., Zhang, R., Yu, D., Dong, G., Liu, J., Geng, Y., et al. (2021). China's Mars exploration mission and science investigation. *Space Science Reviews*, 217(4), 57. <https://doi.org/10.1007/s11214-021-00832-9>
- MacKay, J. R. (1998). Pingo growth and collapse, Tuktoyaktuk Peninsula area, western Arctic coast, Canada: A long-term field study. *Géographie Physique et Quaternaire*, 52(3), 1–53. <https://doi.org/10.7202/004847ar>
- Malin, M. (2007). MRO Context Camera experiment data record level 0 V1.0, MRO-M-CTX-2-EDR-L0-V1.0. *NASA Planetary Data System*. <https://doi.org/10.17189/1520266>
- Maurice, S., Wiens, R. C., Saccoccio, M., Barraclough, B., Gasnault, O., Forni, O., et al. (2012). The ChemCam instrument suite on the Mars Science Laboratory (MSL) rover: Science objectives and mast unit description. *Space Science Reviews*, 170(1–4), 95–166. https://doi.org/10.1007/978-1-4614-6339-9_6
- McGowan, E. M., & McGill, G. E. (2007). *Spatial Correlation of Putative Water Related Features in Cydonia Mensae and Southern Acidalia Planitia*. Seventh International Conference on Mars.
- Meng, Q., Wang, D., Dong, J., Li, W., Yang, X., Yan, D., et al. (2021). High Resolution imaging camera (HiRIC) on China's first Mars exploration Tianwen-1 Mission. *Space Science Reviews*, 217(3), 42. <https://doi.org/10.1007/s11214-021-00823-w>
- Michael, G. G., & Neukum, G. (2010). Planetary surface dating from crater size-frequency distribution measurements: Partial resurfacing events and statistical age uncertainty. *Earth and Planetary Science Letters*, 294(3–4), 223–229. <https://doi.org/10.1016/j.epsl.2009.12.041>
- Oehler, D. Z., & Allen, C. (2010). Evidence for pervasive mud volcanism in Acidalia Planitia, Mars. *Icarus*, 208(2), 636–657. <https://doi.org/10.1016/j.icarus.2010.03.031>
- Pajola, M., Rossato, S., Baratti, E., Mangili, C., Mancarella, F., McBride, K., & Coradini, M. (2016). The Simud-Tiu Valles hydrologic system: A multidisciplinary study of a possible site for future Mars on-site exploration. *Icarus*, 268, 355–381. <https://doi.org/10.1016/j.icarus.2015.12.049>
- Pajola, M., Rossato, S., Baratti, E., Pozzobon, R., Quantin, C., Carter, J., & Thollot, P. (2017). Boulder abundances and size-frequency distributions on Oxia Planum-Mars: Scientific implications for the 2020 ESA ExoMars rover. *Icarus*, 296, 73–90. <https://doi.org/10.1016/j.icarus.2017.05.011>
- Putzig, N. E., Mellon, M. T., Arvidson, R. E., & Kretke, K. A. (2005). Global thermal inertia and surface properties of Mars from the MGS mapping mission. *Icarus*, 173(2), 325–341. <https://doi.org/10.1016/j.icarus.2004.08.017>
- Robbins, S. J., & Hynek, B. M. (2014). The secondary crater population of Mars. *Earth and Planetary Science Letters*, 400, 66–76. <https://doi.org/10.1016/j.epsl.2014.05.005>
- Sefton-Nash, E., Teanby, N., Newman, C., Clancy, R., & Richardson, M. J. I. (2014). Constraints on Mars' recent equatorial wind regimes from layered deposits and comparison with general circulation model results. *Icarus*, 230, 81–95. <https://doi.org/10.1016/j.icarus.2013.11.014>
- Smith, D. E., Zuber, M. T., Frey, H. V., Garvin, J. B., Head, J. W., Muhleman, D. O., et al. (2001). Mars Orbiter Laser Altimeter: Experiment summary after the first year of global mapping of Mars. *Journal of Geophysical Research*, 106(E10), 23689–23722. <https://doi.org/10.1029/2000je001364>
- Sullivan, R., Anderson, R., Biesiadecki, J., Bond, T., & Stewart, H. (2011). Cohesions, friction angles, and other physical properties of Martian regolith from Mars Exploration Rover wheel trenches and wheel scuffs. *Journal of Geophysical Research*, 116(E2), E02006. <https://doi.org/10.1029/2010je003625>
- Tanaka, K. L., Skinner, J. A., Jr., Dohm, J. M., Irwin, R. P., III, Kolb, E. J., Fortezzo, C. M., et al. (2014). *Geologic Map of Mars* (p. 48). US Geological Survey Scientific Investigations Map 3292.
- Wan, W. X., Wang, C., Li, C. L., & Wei, Y. (2020). China's first mission to Mars. *Nature Astronomy*, 4(7), 721. <https://doi.org/10.1038/s41550-020-1148-6>
- Wang, Y. R., & Wu, B. (2019). Active machine learning approach for crater detection from planetary imagery and digital elevation models. *IEEE Transactions on Geoscience and Remote Sensing*, 57(8), 5777–5789. <https://doi.org/10.1109/tgrs.2019.2902198>
- Warner, N. H., Gupta, S., Calef, F., Grindrod, P., Boll, N., & Goddard, K. (2015). Minimum effective area for high resolution crater counting of Martian terrains. *Icarus*, 245, 198–240. <https://doi.org/10.1016/j.icarus.2014.09.024>
- White, J. D. L., & Ross, P.-S. (2011). Maar-diatreme volcanoes: A review. *Journal of Volcanology and Geothermal Research*, 201(1–4), 1–29. <https://doi.org/10.1016/j.jvolgeores.2011.01.010>
- Wu, B. (2022). *Datasets for Zhurong Landing Site on Mars*. <https://doi.org/10.5281/zenodo.5876326>
- Wu, B., Dong, J., Wang, Y., Li, Z., Chen, Z., Liu, W. C., et al. (2021). Characterization of the candidate landing region for Tianwen-1—China's first mission to Mars. *Earth and Space Science*, 8(6), e2021EA001670. <https://doi.org/10.1029/2021ea001670>
- Wu, B., Huang, J., Li, Y., Wang, Y., & Peng, J. (2018). Rock abundance and crater density in the candidate Chang'E-5 landing region on the Moon. *Journal of Geophysical Research: Planets*, 123(12), 3256–3272. <https://doi.org/10.1029/2018je005820>
- Wu, B., Li, F., Hu, H., Zhao, Y., Wang, Y., Xiao, P., et al. (2020). Topographic and geomorphological mapping and analysis of the Chang'E-4 landing site on the far side of the Moon. *Photogrammetric Engineering & Remote Sensing*, 86(4), 247–258. <https://doi.org/10.14358/pers.86.4.247>
- Wu, B., Li, F., Ye, L., Qiao, S., Huang, J., Wu, X., & Zhang, H. (2014). Topographic modeling and analysis of the landing site of Chang'E-3 on the Moon. *Earth and Planetary Science Letters*, 405, 257–273. <https://doi.org/10.1016/j.epsl.2014.09.009>

- Xiao, L., & Wang, C. (2009). Geologic features of Wudalianchi volcanic field, northeastern China: Implications for Martian volcanology. *Planetary and Space Science*, 57(5–6), 685–698. <https://doi.org/10.1016/j.pss.2008.08.005>
- Ye, B., Qian, Y., Xiao, L., Michalski, J. R., Li, Y., Wu, B., & Qiao, L. (2021). Geomorphologic exploration targets at the Zhurong landing site in the southern Utopia Planitia of Mars. *Earth and Planetary Science Letters*, 576, 117199. <https://doi.org/10.1016/j.epsl.2021.117199>
- Zhao, J., Xiao, Z., Huang, J., Head, J. W., Wang, J., Shi, Y., et al. (2021). Geological characteristics and targets of high scientific interest in the Zhurong landing Region on Mars. *Geophysical Research Letters*, 48, 20. <https://doi.org/10.1029/2021gl094903>
- Zou, Y., Zhu, Y., Bai, Y., Wang, L., Jia, Y., Shen, W., et al. (2021). Scientific objectives and payloads of Tianwen-1, China's first Mars exploration mission. *Advances in Space Research*, 67(2), 812–823. <https://doi.org/10.1016/j.asr.2020.11.005>